CORA Cork Open Research Archive
Cartlann Taighde Oscailte Chorcaí

Title	Analysis and design optimization of a compliant robotic gripper mechanism with inverted flexure joints
Authors	Kuresangsai, Pongsiri;Cole, Matthew O. T.;Hao, Guangbo
Publication date	2024-09-02
Original Citation	Kuresangsai, P., Cole, M. O. and Hao, G. (2024) 'Analysis and design optimization of a compliant robotic gripper mechanism with inverted flexure joints', Mechanism and Machine Theory, 202, p.105779 (18pp). https://doi.org/10.1016/j.mechmachtheory.2024.105779
Type of publication	Article (peer-reviewed)
Link to publisher's version	10.1016/j.mechmachtheory.2024.105779
Rights	© 2024, Elsevier Ltd. All rights are reserved, including those for text and data mining, AI training, and similar technologies. This manuscript version is made available under the CC BY-NC-ND 4.0 license. - https://creativecommons.org/licenses/by-nc-nd/4.0/
Download date	2026-11-04 10:13:28
Item downloaded from	https://hdl.handle.net/10468/16432



UCC
University College Cork, Ireland
Coláiste na hOllscoile Corcaigh

Analysis and design optimization of a compliant robotic gripper mechanism with inverted flexure joints

Pongsiri Kuresangsai, Matthew O. T. Cole*, Guangbo Hao

Department of Mechanical Engineering, Chiang Mai University, Chiang Mai 50200, Thailand

School of Engineering and Architecture - Electrical and Electronic Engineering, University College Cork, Ireland

Abstract

Flexure-jointed grippers provide compliant grasping capability, have low-cost and flexible manufacturing, and are insusceptible to joint friction and wear. However, their grasp stiffness can be limited by flexure compliance such that loss-of-grasp is prone to occur for high object loads. This paper examines the application of inverted-flexure joints in a cable-driven gripper that can avoid flexure buckling and greatly enhance grasp stiffness and stability. To analyse behavior, an energy-based kinetostatic model is developed for a benchmark grasping problem and validated by hardware experiments. A multi-objective design optimization study is conducted, considering key metrics of peak flexure stress, grasp stiffness, and cable actuation force. Results show that the inverted-flexure design has significantly higher grasp stiffness (63 % higher in a targeted design optimization) and requires lower actuation forces (>20 % lower in all optimization cases), compared with equivalent direct-flexure designs. An application study is conducted to validate the predicted operating performance under gravity loading of the grasped object. The results demonstrate that stable and high stiffness grasping can be achieved, even under overload conditions that lead to loss-of-grasp for conventional direct-flexure designs.

Keywords: robotic gripper, compliant mechanism, design optimization, flexure joint, grasp stability, kinetostatic modeling

1. Introduction

Compliant grippers are well-suited to robotics applications requiring robust grasping of delicate and/or uncertain objects [1, 2]. Compared with rigid link designs, their construction can involve fewer parts and is suitable for 3-D printing, so that simpler, cheaper and more flexible manufacturing is possible [3]. They can also have reduced susceptibility to contamination and wear compared with conventional bearing-jointed mechanisms [4, 5]. Potential applications can be found in various fields, including manufacturing, agriculture, underwater exploration, and medical robotics [5–8].

Compliant gripper designs can be broadly classified as having distributed compliance [5, 8], as exemplified by the adaptive finger commercialized by Festo [9], or having localized compliance which produces joint-like behaviour similar to the segmented fingers in humans [10–12]. The present study focuses on a multi-fingered gripper with compliant joints that can be designed for large motion range in order to envelop an object and thereby achieve robust grasping with uncertain object shape and size [13, 14]. For such designs, however, the stress/strain developed within the joints during operation can be a main limiting factor for performance

*Corresponding author

Email addresses: pongsiri_kuresangsai@outlook.com (Pongsiri Kuresangsai), motcole@dome.eng.cmu.ac.th (Matthew O. T. Cole), G.Hao@ucc.ie (Guangbo Hao)

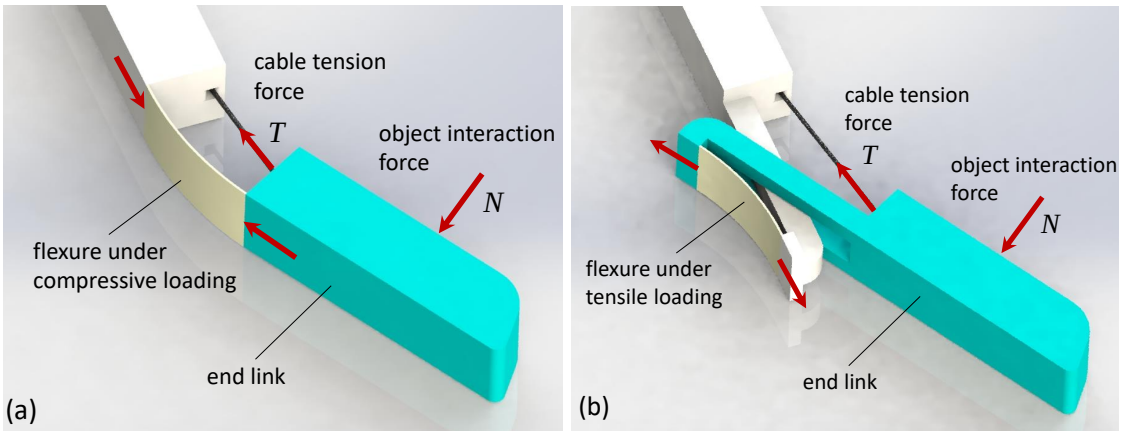


Figure 1: Cable-driven compliant joints: (a) conventional direct flexure design (b) inverted flexure design.

and functionality [15, 16]. Therefore, it is important to understand the influence of the structure layout and joint topology on gripper performance, and this is still an open area for research.

A further issue in gripper design problems is the stiffness and stability of grasping [17]. In previous work, an underactuated two-finger gripper was investigated by Kragten et al. [18] using an energy-based model to examine design requirements for stable grasping of a circular object between curved distal phalanges. A simple gripper with two flexible beam fingers was considered in [19], where the effect of object size, joint stiffness, preload, and beam-curvature on grasp stability were evaluated from the concavity of the potential function. In recent work by Okken et al. [20], a compliant two-finger gripper with fourteen crossed-flexure hinges was developed and geometrically optimized to achieve stable grasping of circular objects with five-point contact.

In previous research on flexure-joint design, a main objective has been to achieve large motion range with low stress concentration. To mimic conventional joints, flexure-based designs should possess low stiffness in desired directions of motion, but provide high-stiffness resistance against undesired deflections [4, 14, 16, 21]. The shape optimization for a flexure-based fingered gripper was considered in [3], where the Nelder Mead direct search method was applied to minimize the ratio of peak stress to grasping force. In [22], topology optimization was applied to the structure of a compliant gripper to achieve a large bending range, with the aim of handling a variety of objects without sliding. An energy-based modelling approach was applied to analyze the joint stiffness of a flexure-based gripper, and determine suitable link-length ratios to achieve large workspace in [23]. Application to mini-invasive surgery was considered in [24], where the multi-objective design optimization problem was studied for a miniature monolithic compliant gripper.

Flexure-based gripper designs have commonly used direct-flexure joints, as illustrated in Fig. 1a. For this design, grasp stability tends to be reduced when the object interaction force N is increased, as this introduces compressive axial loading on the flexure. At critical compressive loads, the flexure joint can buckle, causing a loss of grasp stability [25]. In this paper, an inverted flexure joint is considered with the structure shown in Fig. 1b. For this design, the external force N and cable force T produce a tensile axial load on the flexure that will inhibit buckling and therefore allow higher external interaction loads compared with the more conventional joint design [26, 27]. Previously reported applications include compliance-based universal joints [28] and cable-driven surgical grippers [29].

Although gripper designs based on inverted flexure joints are conceptually simple, their grasping behaviour is not straighforward to predict, or to optimize. As the joint flexures must be sufficiently long and thin to allow the large angular deflections necessary for closed stable grasping, the behaviour cannot be predicted by simple lumped compliance models and instead requires a realistic non-linear model of the large deformation behaviour. This contrasts with previous compliant gripper mechanisms that can be simulated and designed using simpler pseudo-rigid-body models, where flexures are treated as discrete compliance elements [30]. Within the existing literature, model-based analysis of object grasping with an inverted flexure

joint mechanism, and its utilization in parametric design optimization, has not been reported. Previous work by the authors considered the performance analysis of a gripper mechanism with the conventional direct flexure joints [25], highlighting grasp instability as a main limitation. The present work examines the achievable performance of the inverted flexure joint design using an experimentally validated elasto-kinematic gripper model for a benchmark grasping problem. Furthermore, a methodology for design optimization is proposed to maximize performance, with this also allowing direct comparisons with optimized direct-flexure designs.

The new contributions are summarised as follows:

1. An energy-based elasto-kinematic model is defined for a cable-driven inverted flexure joint gripper that accounts explicitly for object interaction and has high computational efficiency suitable for simulation-based design optimization.
2. An experimental and numerical study is performed that examines model validity and gripper performance for a chosen design case. This includes a sensitivity analysis with respect to two main sources of uncertainty: object contact friction and compliance effects associated with non-rigid link connections and cable compliance.
3. A model-based design optimization methodology is proposed that uses a weighted sum of metrics for effective grasp stiffness, actuation force and peak flexure strain, and a comparative study of achievable performance for direct flexure and inverted flexure joint gripper designs conducted.

Within the paper, Section 2 presents the energy-based modeling approach used to predict kinetostatic behavior and grasp stability limits. Section 3 describes the simulation-based evaluation of gripper performance, and the construction of feasible design sets for a benchmark grasping task. Results for a specific inverted flexure gripper design are also presented and verified through experiments. Section 4 presents the design optimization study, while Section 5 presents the application study and comparative results. The final section provides conclusions.

2. Grasping simulation model

Various approaches have been considered for the modeling of flexure-based mechanisms, a review of which can be found in [31]. For kinetostatic modeling of large deformation behaviour, with consideration of buckling, this study adopts the smooth (polynomial) curvature model introduced in [32]. This method has low computational complexity, yet can achieve high accuracy prediction of large deflections (up to 90 degrees in bending) and may be extended for multi-joint mechanisms as reported in [33]. Liu et al. [34] examined the accuracy and computational efficiency of the smooth curvature model, showing that accurate computation of buckling solutions for a bistable mechanism could be achieved significantly faster than with a non-linear finite element model. Therefore, the approach is well-suited to simulation-based design optimization problems.

2.1. Lagrangian formulation

Suppose a planar mechanism has n_l rigid links with center of mass (CoM) positions defined by $\boldsymbol{z}_i = [x_i\, y_i\, \theta_i]^T$ in a global inertial frame. The set of link coordinate is $\boldsymbol{z}^T = [\boldsymbol{z}_0^T, \boldsymbol{z}_1^T, \boldsymbol{z}_2^T, ..., \boldsymbol{z}_{n_l}^T]$ where $\boldsymbol{z}_0$ denotes the position coordinates of the grasped object. Flexure members, indexed by $k = 1, ..., n_k$, are employed as joint elements connecting pairs of rigid links. The elastic energy of the flexure member k is given by $U_k(\boldsymbol{q}_k)$, where $\boldsymbol{q}_k$ is the vector of flexure deformation variables.

A set of n_m kinematic constraint equations relating to contact interactions, as well as flexure and cable attachment conditions, can be introduced in the general form $\mathcal{K}_m(\boldsymbol{z}, \boldsymbol{q}) = \boldsymbol{0}$, where $m = 1, ..., n_m$ and $\boldsymbol{q}^T = [\boldsymbol{q}_1^T, \boldsymbol{q}_2^T, ..., \boldsymbol{q}_{n_k}^T]$. Further details on formulating this set of constraints for a specific design case will be given in Section 2.3. According to the defined notation, the Lagrangian for the whole mechanism has the form

$$\mathcal{L} = \frac{1}{2} \sum_i \dot{\boldsymbol{z}}_i^T M_i \dot{\boldsymbol{z}}_i - \sum_k U_k(\boldsymbol{q}_k) - \sum_m \lambda_m \mathcal{K}_m(\boldsymbol{z}, \boldsymbol{q}) \tag{1}$$

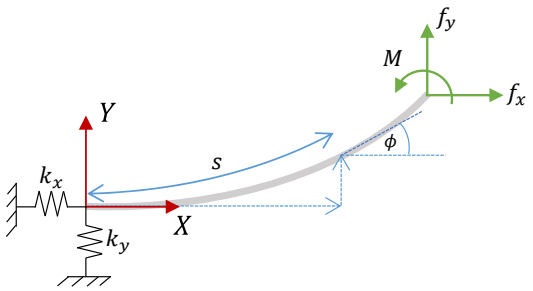


Figure 2: Flexure model notation.

where M_i is the constant mass matrix for link i and λ_m is the Lagrange multiplier for the m^{th} constraint. Defining $\boldsymbol{\lambda} = [\lambda_1, .., \lambda_{n_m}]^T$, the vector of all generalized coordinates (configuration variables) can be concatenated as $\boldsymbol{\eta}^T = [\boldsymbol{z}^T \, \boldsymbol{q}^T \, \boldsymbol{\lambda}^T]$ so that equation (1) can be expressed in the matrix form:

$$\mathcal{L}(\boldsymbol{\eta}) = \frac{1}{2}\dot{\boldsymbol{z}}^T M \dot{\boldsymbol{z}} - U(\boldsymbol{q}) - \boldsymbol{\lambda}^T \boldsymbol{\mathcal{K}}(\boldsymbol{z}, \boldsymbol{q}) \tag{2}$$

Applying Lagrange's equation $\frac{d}{dt}\left(\frac{\partial \mathcal{L}}{\partial \dot{\boldsymbol{\eta}}_i}\right) - \frac{d\mathcal{L}}{d\boldsymbol{\eta}_i} = \boldsymbol{Q}_i$ for each generalized coordinate (where $\boldsymbol{Q}_i$ is the corresponding external force, if present), gives:

For rigid body coordinate (with respect to $\boldsymbol{z}$):

$$M\ddot{\boldsymbol{z}} + (\nabla_z \boldsymbol{\mathcal{K}})^T \boldsymbol{\lambda} = \boldsymbol{Q}_i \, , i = 1, .., n_l \tag{3}$$

For flexure variables (with respect to $\mathbf{q}$):

$$\nabla_q U + (\nabla_q \boldsymbol{\mathcal{K}})^T \boldsymbol{\lambda} = \mathbf{0} \tag{4}$$

For constraint functions (with respect to $\boldsymbol{\lambda}$):

$$\boldsymbol{\mathcal{K}}(\boldsymbol{z}, \boldsymbol{q}) = \mathbf{0} \tag{5}$$

For quasi-static modeling, where the dynamic effects from link and object motion are negligible, the term $M\ddot{\boldsymbol{z}}$ in Eq. (3) can be neglected. In this case, Eqs (3)-(5) form a set of simultaneous algebraic equations which may be solved with a multi-dimensional root-finding algorithm such as Newton's method. This allows simulation of the gripper and object equilibrium configuration, and associated stability properties, for any specified loading condition.

2.2. Flexure deformation model

To model elastic deformation of the flexure elements, an idealized inextensible thin beam may be considered for which bending is dominant and shearing is negligible. Under the action of end-loads $\boldsymbol{f} = [f_x \, f_y \, M]^T$, the tangent angle $\phi(s)$ will vary with distance along the neutral axis $s \in [0, L]$ (where L is the beam length), as illustrated in Fig. 2. The beam curvature $\phi'(s)$ may be expressed using a superposition of smooth basis functions ψ_n, parameterized by the coefficients α_n:

$$\frac{d\phi}{ds} = \phi'(s, \boldsymbol{\alpha}) = \sum_{n=0}^{N} \alpha_n \psi_n(s) \tag{6}$$

Previous research has shown that the set of shifted Legendre polynomials is a good choice for ψ_n, allowing low order, yet high accuracy prediction of large deformation [32]. The total elastic energy, as derived from

Euler-Bernoulli theory, can be expressed

$$\begin{aligned} U(\boldsymbol{q}) &= \tfrac{1}{2}k_x\Delta_x^2 + \tfrac{1}{2}k_y\Delta_y^2 + \tfrac{1}{2}EI\int_0^L \left(\phi'(s,\boldsymbol{\alpha})\right)^2 \mathrm{d}s \\ &= \tfrac{1}{2}\boldsymbol{q}^T K \boldsymbol{q} \end{aligned} \tag{7}$$

where E is the material Young's modulus and $\boldsymbol{q}^T = [\Delta_x\ \Delta_y\ \boldsymbol{\alpha}^T]$ is the vector of flexure deformation variables. The extra deflection coordinates Δ_x and Δ_y are introduced to allow small deflections of the attachment point. This is beneficial for avoiding singularity issues that arise when solving numerically due to the assumption of constant flexure length [33]. In this case, high values for the stiffness coefficients k_x and k_y can be chosen so that the effect on the equilibrium solution is negligible. Lower values of k_x and k_y may also be appropriate in cases where compliance in the attachment points (e.g. due to non-rigid links) is significant. For a uniform rectangular cross-section, the second moment of area is $I = \frac{1}{12}wt^3$ where w is the width and t is the thickness of the flexure. Adopting the first three shifted Legendre polynomials for the basis functions ψ_n as a basis set for Eq. (6) yields

$$\phi'(s,\alpha) = \frac{\alpha_0}{L} + \frac{\alpha_1}{L}\left(\frac{2s}{L} - 1\right) + \frac{\alpha_2}{L}\left(\frac{6s^2}{L^2} - \frac{6s}{L} + 1\right) \tag{8}$$

The corresponding stiffness matrix K in Eq. (7) is given by

$$K = \begin{bmatrix} k_x & 0 & 0 & 0 & 0 \\ 0 & k_y & 0 & 0 & 0 \\ 0 & 0 & \beta & 0 & 0 \\ 0 & 0 & 0 & \beta/3 & 0 \\ 0 & 0 & 0 & 0 & \beta/5 \end{bmatrix}, \text{ with } \beta = \frac{Et^3w}{12L} \tag{9}$$

The position of the flexure tip relative to the X-Y frame fixed at the flexure root is given by $\boldsymbol{g}(\boldsymbol{q}) = [x_L(\boldsymbol{q})\, y_L(\boldsymbol{q})\, \phi_L(\boldsymbol{q})]^T$, where

$$x_L(\boldsymbol{q}) = \Delta_x + \int_0^L \cos\left(\phi(s,\boldsymbol{\alpha})\right) \mathrm{d}s \tag{10}$$

$$y_L(\boldsymbol{q}) = \Delta_y + \int_0^L \sin\left(\phi(s,\boldsymbol{\alpha})\right) \mathrm{d}s \tag{11}$$

$$\phi_L(\boldsymbol{q}) = \int_0^L \phi(s,\boldsymbol{\alpha}) \mathrm{d}s \tag{12}$$

These equations can be integrated numerically, for example by Gauss-Legendre quadrature, to determine their parametric dependency on $\boldsymbol{q}$ (see [32]).

Stress occurring along the flexure must also be predicted to assess the possibility of failure. The maximum bending stress will occur at the point of maximum curvature ϕ'_{max}. The location of this point may be at the root or tip of the flexure, or at points along its length $s^\star \in (0, L)$ where $\phi'' = 0$. Accordingly,

$$\phi'_{max} = \max\{|\phi'(0,\boldsymbol{\alpha})|, |\phi'(s^*,\boldsymbol{\alpha})|, |\phi'(L,\boldsymbol{\alpha})|\} \tag{13}$$

An upper bound on the total stress can be calculated conservatively by summing the maximum bending stress $\frac{1}{2}Et\phi'_{max}$ with an upper bound on the maximum axial stress; $\sigma_{axial} = F_{axial}/wt$, where $F_{axial} \leq \sqrt{f_x^2 + f_y^2}$, so that

$$\sigma_{max} \leq \frac{Et}{2}\phi'_{max} + \frac{1}{wt}\sqrt{f_x^2 + f_y^2} \tag{14}$$

The relative importance of the two stress contributions will depend on the joint design and loading conditions. For the direct flexure joint design in Fig. 1a, the bending-induced stress in the slender flexure is usually more dominant than the axial compressive stress. This is true when large bending deformation arises during grasping and instability occurs at high loads, before the axial load effect becomes significant. However, for the inverted flexure design in Fig. 1b, the magnitude of axial tension can be larger, and the axial stress term in Eq. (14) is important for correct analysis.

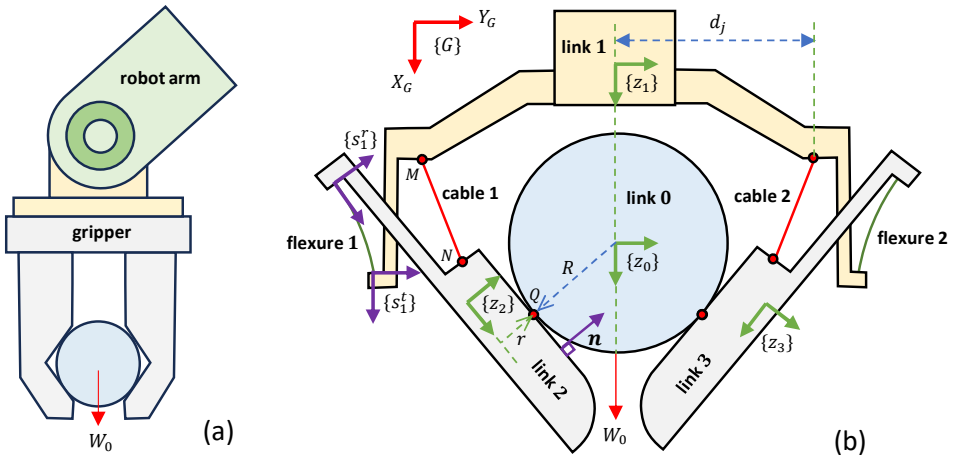


Figure 3: Benchmark grasping problem for a two finger gripper: (a) Application scenario with conventional gripper design (b) Geometry of inverted flexure joint gripper.

2.3. Geometry of benchmark problem

Two-finger grippers are commonly used for robotic handling of small parts, as illustrated for a conventional gripper holding a cylindrical object in Fig. 3a. A benchmark grasping problem may be defined for a gripper with two flexure-jointed fingers holding an object of circular cross section under vertical load W_0, as shown in Fig. 3b. The effect of in-plane forces may be considered, as appropriate for operation in a vertical plane when gravity and acceleration forces on the object are also in-plane. For 3-D manipulation, the effect of out-of plane loads on joint deflections may also become important. However, the out-of-plane rigidity of the joint can be made significantly higher than the in-plane rigidity by using flexures of sufficient width [35]. Therefore, in-plane kinetostatic analysis can be reasonably used as a basis to assess gripper performance.

A grasping model is defined explicitly according to the geometry in Fig. 3b, following the general formulation given in Section 2.1. The gripper has a rigid palm (link 1) and two fingers (links 2 and 3), where each finger link is connected with the palm by a cable and a thin beam flexure. The cable length is controlled by an actuator to achieve closed grasping of the circular object. The ends of the cables are attached to pins fixed on the finger links, as indicated by point N, and constrained to pass though a guide point M on link 1. The circular grasped object, which is assumed to be rigid, can move along the link surfaces under the action of an external load W_0.

The actuation cable connecting links 1 and 2 can be defined by the position of points M and N, given by vectors $\boldsymbol{p}_M = [x_M, y_M]^T$ and $\boldsymbol{p}_N = [x_N, y_N]^T$ in the global Cartesian frame $\{G\}$:

$$\mathcal{C}_1(\boldsymbol{z}) = |\boldsymbol{p}_N(\boldsymbol{z}_2) - \boldsymbol{p}_M(\boldsymbol{z}_1)| - L_{c1} = 0 \tag{15}$$

Here, L_{c1} is the cable length. The same form of constraint is applied for the cable connecting links 1 and 3.

Suppose the position of the object CoM $\{z_0\}$ and finger CoM $\{z_i\}$ in the fixed global frame are given by $\boldsymbol{p}_{z_0} = [x_0, y_0]^T$ and $\boldsymbol{p}_{z_i} = [x_i, y_i]^T$. The contact constraint relating the position of the object (link 0) and finger links ($i = 2, 3$) can be derived by projecting the relative position vector $\boldsymbol{p}_{z_0} - \boldsymbol{p}_{z_i}$ to the direction of the unit normal vector $\boldsymbol{n}$ at the contact point Q between the rigid link and circular object. The projected distance will take a constant value $R + r$ where R is the radius of the object and r is the offset distance, as shown in Fig. 3. The corresponding constraint function has the form

$$\mathcal{O}_{0j}(\boldsymbol{z}) = \left(\boldsymbol{p}_{z_0}(\boldsymbol{z}_0) - \boldsymbol{p}_{z_i}(\boldsymbol{z}_i)\right).\boldsymbol{n}(\boldsymbol{z}_i) - (R + r) = 0 \tag{16}$$

To derive the flexure constraint functions, consider the flexures ($k = 1, 2$) which join the palm link 1 to the finger links ($i = 2, 3$). Suppose $\boldsymbol{s}_k^r = [x_k^r, y_k^r, \theta_k^r]^T$ and $\boldsymbol{s}_k^t = [x_k^t, y_k^t, \theta_k^t]^T$ are the positions of the root and

tip in the global frame. The relative position in the global frame can be mapped to the root frame $\{s_k^r\}$ and related to the flexure deformation variables via the tip position vector $\boldsymbol{g}(\boldsymbol{q})$ defined by equations (10)-(12). This yields

$$\boldsymbol{\mathcal{F}}_k(\boldsymbol{z}, \boldsymbol{q}_k) = \tilde{R}(-\theta_i - \theta_f)\left(\boldsymbol{s}_k^t(\boldsymbol{z}_1) - \boldsymbol{s}_k^r(\boldsymbol{z}_i)\right) - \boldsymbol{g}_k(\boldsymbol{q}_k) = \boldsymbol{0} \tag{17}$$

where θ_f is the flexure angle (see Fig. 4) and $\tilde{R}$ is the rotation matrix:

$$\tilde{R}(\theta) = \begin{bmatrix} \cos\theta & -\sin\theta & 0 \\ \sin\theta & \cos\theta & 0 \\ 0 & 0 & 1 \end{bmatrix} \tag{18}$$

Explicit formulas for the position vectors used in the constraint equations (15)-(17) are given in the appendix.

Kinematic constraints from Eqs (15)-(17) can be combined for the whole mechanism as $\boldsymbol{\mathcal{K}}(\boldsymbol{z}, \boldsymbol{q}) = \{\mathcal{C}\,\mathcal{O}\,\boldsymbol{\mathcal{F}}\} = \boldsymbol{0}$. The corresponding Lagrange multipliers $\boldsymbol{\lambda} = \{T\,N\,\boldsymbol{f}\}$ can be interpreted as cable force, normal contact force and flexure end-loads, respectively, in accordance with the virtual work principle. Equations (3)-(5) allow solution of the gripper and object motions under arbitrary loading conditions that involve physically plausible deflections.

2.4. Effective grasp stiffness

The effective grasp stiffness of the gripper mechanism can be evaluated under the assumption of unidirectional loading of the object along the symmetry axis, as shown in Fig. 3b. The applied external load W_0 will produce object motion such that the contact points slide along the link surfaces and elastic deflections of the flexures occur. It is assumed here that the length of the actuation cables remains fixed and slow quasi-static motion occurs ($\ddot{\boldsymbol{z}} \approx 0$). The set of Lagrange equations (3)-(5) can then be expressed in the vector form:

$$\boldsymbol{\Theta}(\boldsymbol{\eta}, W_0) = \nabla_\eta \mathcal{L} + \boldsymbol{Q} = \boldsymbol{0} \tag{19}$$

where, for the considered object loading, only one element of $\boldsymbol{Q}$ corresponding to W_0 is non-zero. For equilibrium solutions satisfying Eq. (19), the configuration-dependent directional grasp stiffness can be defined as

$$K_e = \frac{\mathrm{d}W_0}{\mathrm{d}x_0} \tag{20}$$

where x_0 is the displacement of the object in the direction of the load W_0. This stiffness measure directly reflects the displacement response of the grasped object to a change in the applied load. Therefore, the positioning of the grasped object becomes unstable if $K_e \leq 0$. To compute this stiffness measure, a small change in $\boldsymbol{\Theta}(\boldsymbol{\eta}, W_0)$ may be considered due to a small perturbation in W_0. From Eq. (19), this must satisfy

$$\boldsymbol{\Theta}(\boldsymbol{\eta} + \mathrm{d}\boldsymbol{\eta}, W_0 + \mathrm{d}W_0) = \nabla\nabla_\eta \mathcal{L}\mathrm{d}\boldsymbol{\eta} + \mathrm{d}\boldsymbol{Q} = \boldsymbol{0} \tag{21}$$

where $\nabla\nabla_\eta \mathcal{L}$ is the Hessian matrix for $\mathcal{L}$. Therefore,

$$\mathrm{d}\boldsymbol{\eta} = -\left(\nabla\nabla_\eta \mathcal{L}\right)^{-1} \mathrm{d}\boldsymbol{Q} \tag{22}$$

The matrix $\boldsymbol{C} = -\left(\nabla\nabla_\eta \mathcal{L}\right)^{-1}$ is the generalized compliance matrix for the mechanism. Also, we may select the element of $\boldsymbol{\eta}$ corresponding to x_0 to obtain the scalar stiffness measure:

$$K_e = \frac{\mathrm{d}W_0}{\mathrm{d}x_0} = \frac{\mathrm{d}\boldsymbol{Q}_m}{\mathrm{d}\boldsymbol{\eta}_n} = \frac{1}{C_{nm}} \tag{23}$$

The grasped object is stable and robustly held if K_e takes large positive values. It is also implied that the object displacement will become sensitive to the load value near the critical load when $K_e = 0$ and the gripper cannot maintain hold of the target object when exceeding the critical load. Consequently, the effective grasp stiffness K_e can be usefully considered as a design metric that should be maximized in order to maximize the stability margin for avoidance of loss-of-grasp.

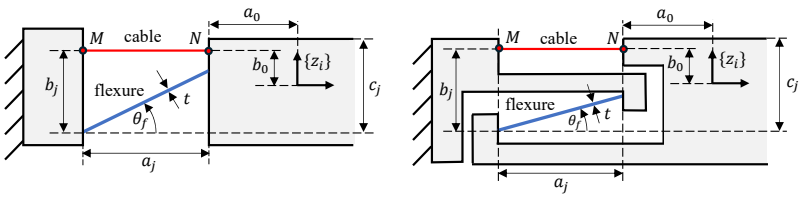


Figure 4: Geometry layout and design parameters for (a) direct flexure and (b) inverted flexure joint designs.

Table 1: Case study design parameters.

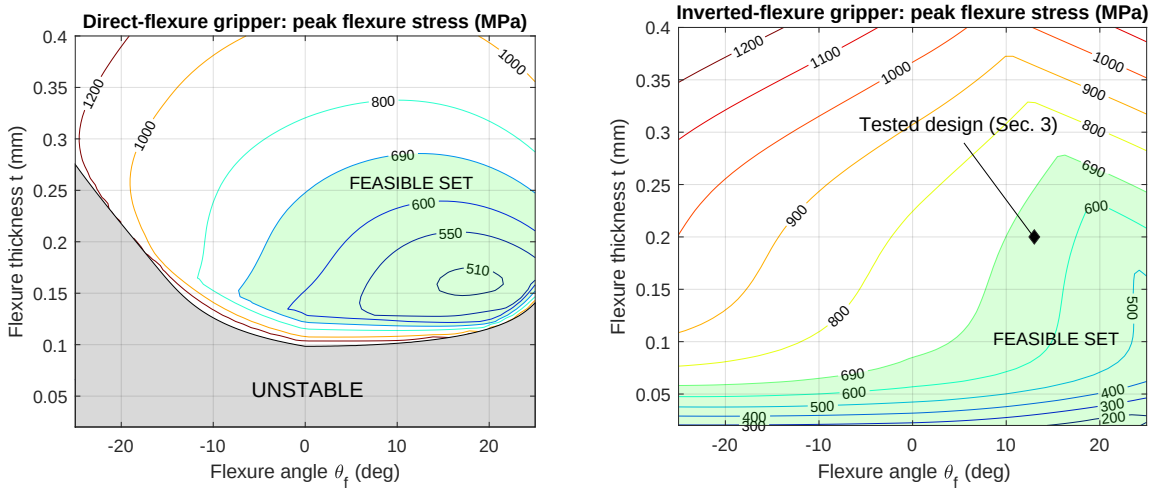
Parameter	Symbol	Value	Units
Gripper half-width	d_j	32.95	mm
Joint length	a_j	20.0	mm
Joint depth	b_j	10.0	mm
Gripper surface offset	c_j	15.0	mm
Joint flexure width	w_j	10.0	mm
Flexure stress limit	σ_{lim}	690	MPa
Flexure modulus	E	125	GPa

3. Design analysis and verification

3.1. Predicted grasping performance

The simulation model and analysis methods presented in Section 2 can be used to predict the performance of a given gripper design during object grasping. The joint geometries for the two design types are shown in Fig. 4. Although the characteristics of the two designs are different, topologically they are equivalent, differing only by the orientations and attachment locations of the joint flexures. Consequently, the mathematical model described in Section 2 can be applied to both designs. For case study, the overall joint properties were fixed according to the parameter values shown in Table 1. The flexure length is $L = a_j/\cos\theta_f$ in all cases. The flexure material properties are for beryllium copper grade C17200. In general, the normal operating limit for the flexure stress σ_{lim} should be set lower than the endurance limit in order to account for fatigue. However, the material yield strength σ_y is still relevant to overload situations that may occur only occasionally. In practice, a stress limit value should be adopted that is appropriate to the material and intended number of operating cycles.

The gripper design types were evaluated and compared by considering a nominal grasping task with a circular object of radius 20 mm and initial finger link angle of 40°. Simulations involved increasing the object displacement in small increments until the target load value of $\widehat{W}_0 = 3$ N was reached. As the overall length and width of the joint are fixed to achieve a suitably compact size, the important remaining design variables are the flexure angle θ_f and thickness t. The influence of these parameters can be seen from Fig. 5, which shows the peak stress occurring for different designs generated within the parameter ranges $t \in (0.02, 0.4)$ mm and $\theta_f \in (-25°, 25°)$ (based on uniform distribution of random values). The simulation results for each case were also used to evaluate whether grasp instability occurred (i.e. the effective grasp stiffness defined by Eq. (23) took negative values) or the flexure stress limit was exceeded ($\sigma_{max} > 690$ MPa). If neither of these occurred, the design was considered acceptable i.e. within the feasible sets indicated in the figure. It can be seen that, for the direct-flexure design, there is a clear optimum point for minimizing the peak stress (close to $t = 0.16$ mm, $\theta_f = 17°$). However, for the inverse flexure case, increasing the angle and decreasing the thickness of the flexure tend to reduce the peak stress. Therefore, other practical considerations must come into play when optimizing the design. The complexity of the problem is increased when a range of different grasping conditions must be considered in the design selection/optimization. In Section 4 of the paper, a simulation-based optimization procedure is proposed to design the gripper by considering a trade-off between key performance metrics.



(a) (b)

Figure 5: Contours of peak flexure stress over the joint design space for (a) direct-flexure designs (b) inverted-flexure designs. Results are based on simulation of the benchmark grasping task when the initial finger link angle is 40 degrees and object radius is 20 mm.

For the direct flexure designs, there is a large instability set associated with flexure joint buckling at large loads (Fig. 5a). In these cases, the axial compressive load on the flexure tends to increase with increasing object load, causing K_e to decrease until grasp instability occurs. Simulation results are shown in Fig. 6 for designs with $\theta_f = 0°$ and $t = 0.07$ mm. For the direct-flexure design, the maximum possible load is $W_0 = 1.12$ N, corresponding to the stability limit when $K_e = 0$. Figure 7a shows the mechanism configuration corresponding to this stability limit. For the inverted flexure designs, there are no design cases that exhibit grasp instability (Fig. 5b). Instead, there is a trend of increasing grasp stiffness with increasing object load (see Fig. 6).

3.2. Model uncertainty

As the inverted flexure joint gripper exhibits higher grasp stiffness compared with the direct flexure design, effects from compliance in the links, especially at the attachment points of the cables, can be more significant. To accurately model link compliance would require the use of complex non-linear finite element models. However, such models are ill-suited to simulation-based design optimization due to the lengthy solving times [34]. An alternative approach adopted here is to introduce a lumped compliance at the link connection points for both the flexures and actuation cables. The model follows that described in Section 2 but uses modified values for k_x and k_y that incorporate link compliance via a representative isotropic compliance C_l localized at at the attachment points:

$$\tilde{k}_x = \left(k_x^{-1} + C_l\right)^{-1}, \; \tilde{k}_y = \left(k_y^{-1} + C_l\right)^{-1}$$

Friction between the object and finger surfaces will also occur in practice, affecting the equilibrium state of the gripper. For a given object load, the friction force during equilibrium conditions will be indeterminate as there is a finite set of different equilibrium states corresponding to different friction force values below the limiting static value. To account for a limiting static friction, the Lagrange equation (3) can be easily modified: As the location of the contact point along the finger link is already included as a generalized coordinate, the friction force $F = -\mu N$ can be added as a corresponding generalized force, i.e. element of the vector $\boldsymbol{Q}$.

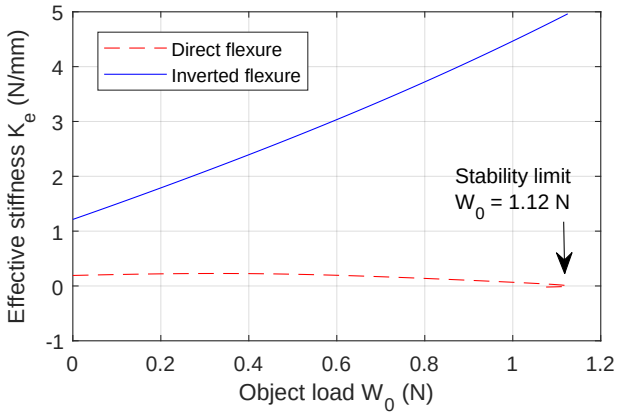


Figure 6: Dependency of effective grasp stiffness on object load for equivalent direct flexure and inverted flexure gripper designs ($\theta_f = 0°$, $t = 0.07$ mm).

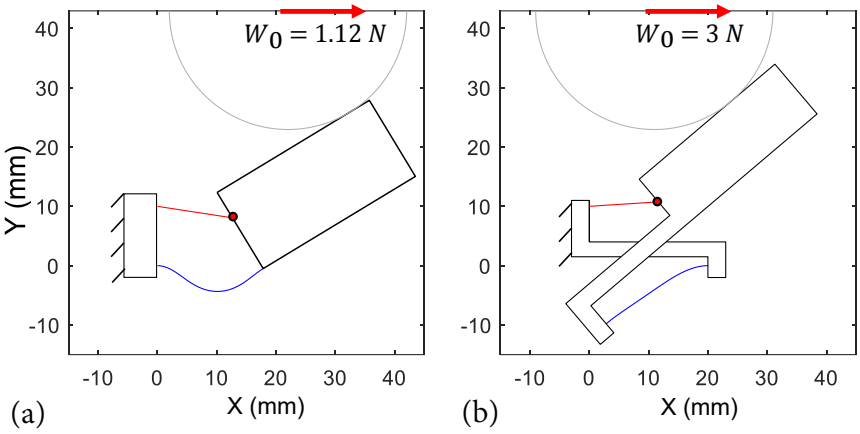


Figure 7: Deformed configurations for example design cases with $\theta_f = 0°$, $t = 0.07$ mm, and initial finger angle 40°: (a) conventional direct flexure design and (b) inverted flexure design.

3.3. Experimental validation

Experimental validations of grasping performance for a direct flexure gripper design were presented previously in [25]. Therefore, the experimental result in this section focus on the inverted flexure gripper design. The hardware setup for the experiments involved a specially designed test rig operating in the horizontal plane, as shown in Fig. 8. The testing procedure was devised for verifying the model-based load-displacement results and for establishing the achievable performance of the inverted-flexure design under controlled conditions. The motion of the finger links was controlled by the joint cables, with one end fixed to the finger link by a pin joint (to reduce cable bending effects) and the other end attached to a guide bar. Displacement of the guide bars was controlled by screw shafts and linear guides. The cable lengths were inferred from measurement of the guide bar displacements using digital micrometers. Motion of the circular grasped object was constrained by a linear guide, where the grasped object ($R = 20$ mm) was displaced by a threaded push-rod attached to a digital force sensor having measurement range $0 - 10$ N and resolution 0.01 N. Consequently, the relation between the measured equilibrium object load and the controlled displacement could be recorded and used to evaluate the grasp stiffness and stability, as defined by Eq. (20).

For the tested design, the gripper links and grasped object were fabricated by 3-D printing using PLA material. The material of the flexure joints was beryllium copper grade C17200 with the material properties given in Table 1. The joint parameters were $\theta_f = 13°$ and $t = 0.2$ mm, as indicated in Fig. 5b. Initial tests

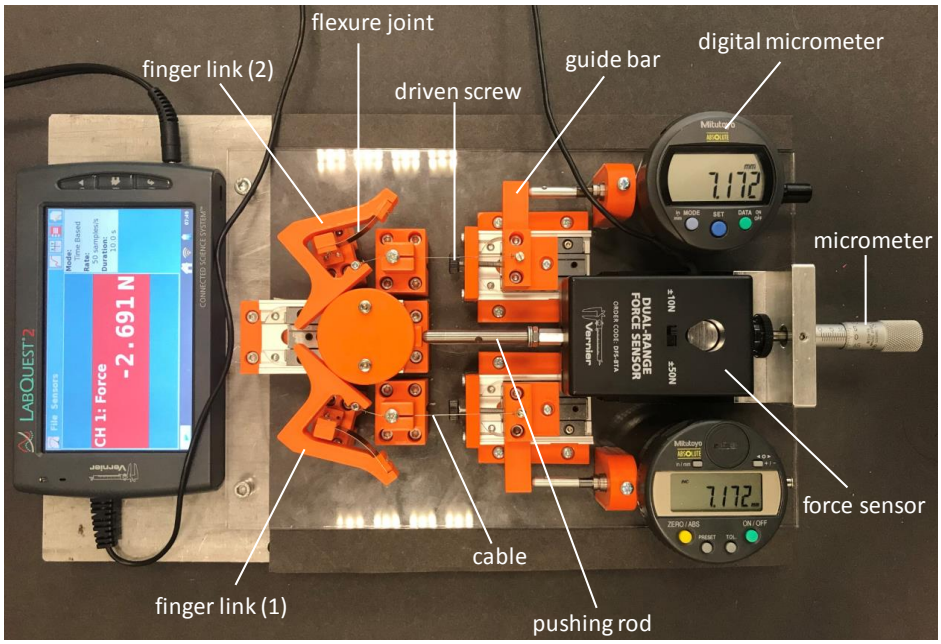


Figure 8: Experimental setup for grasp performance evaluation.

were performed to evaluate kinematic behavior without object contact by measuring the relation between the cable displacement and finger angles. The theoretical predictions were obtained as equilibrium solutions to Eq. (19) when $\boldsymbol{Q} = \mathbf{0}$ ($W_0 = 0$). For the experiments, the finger link angles were measured using a digital camera and image post-processing (within $\pm 1^\circ$ accuracy). The experimental results in Fig. 9 show good agreement with the theoretical results, with small differences being partly attributable to manufacturing errors.

To determine the relation between object load and object displacement, the displacement was increased in small steps and the applied load recorded under static equilibrium. Experimental results are shown in Fig. 10 for three cases with different initial finger angles ($\theta_l = 30^\circ, 35^\circ, 40^\circ$), together with the model-based results. Model uncertainty is accounted for by considering a range of friction coefficient values ($\mu = 0 \rightarrow 0.05$) and link compliance values ($C_l = 0.0017 \rightarrow 0.0036$ mm/N). The upper bounds on the predicted force therefore correspond to the maximum friction and minimum link compliance, while the lower bounds correspond to zero friction and the maximum link compliance. The experimental results agree closely with the nominal model, for which $\mu = 0$ and $C_l = 0.0017$ mm/N. For the experiments, the object-finger contact involved smooth surfaces of PLA with low friction. In addition, small relaxation displacements at the contact points may cause the friction force to drop in steady equilibrium. The results suggest that link compliance at the cable and flexure attachment locations has a more significant role in the measured behavior.

4. Design optimization study

4.1. Simulation-based optimization procedure

Parametric optimization methods can be applied to a candidate flexure-jointed gripper design to improve grasping performance over a range of different object sizes and loading conditions. In previous research on flexure-jointed mechanisms and grippers, various performance metrics have been identified, including peak-stress in flexure joints, required actuation forces, and gripper motion range [15, 22, 24]. Others design requirements could be considered such as maximizing grasping force [3] and out-of-plane stiffness [16], which can also help to improve grasping robustness. In the present work, the optimization procedure focuses on

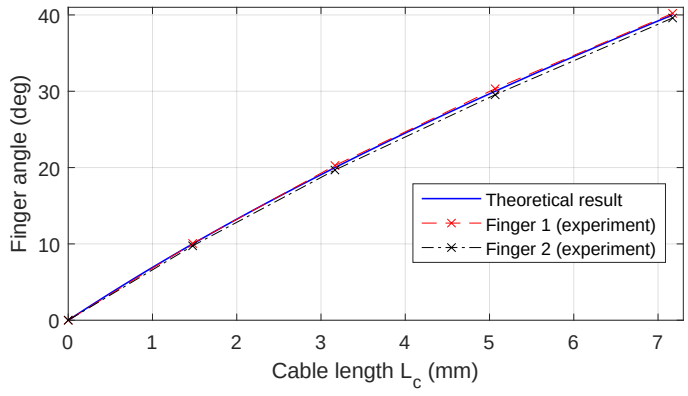


Figure 9: Kinematic behavior without object interaction: Theory and experiment.

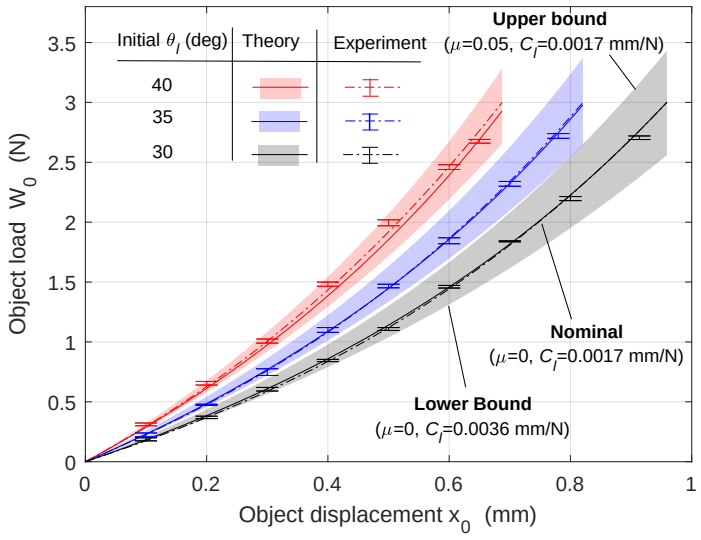


Figure 10: Experimental and theoretical results for grasped object load versus displacement with different initial finger angles.

the two key metrics defined in Section 3 (effective grasp stiffness and peak flexure stress), in combination with the cable actuation force.

With rapid simulation times (approximately 1.2 seconds per simulation run on personal computer with Intel CORE i7 5500U processor), the theoretical model could be used to evaluate the identified performance metrics for a large population of candidate designs over a range of different grasping tasks i.e. different object geometries and initial positions. For the optimization procedure, nine grasping tasks involving three different object sizes (radii $R = 15$, 20, and 25 mm) and three different initial finger angles ($\theta_l = 30^\circ, 35^\circ, 40^\circ$) were considered, as illustrated in Fig. 11. The simulations followed the method described in Section 3.1 with object load varied from zero to a maximum value of $\widehat{W}_0 = 3$ N. As friction tends to increase the grasp stiffness and maximum stable load, it was considered to be negligible – this being the most conservative assumption.

The steps 1-4 of the optimization procedure are described in general terms (in italics), followed by specific details for the case at hand:

Step 1: Generate candidate design set. *An initial large population of candidate designs is generated within a finite set defined by the allowed range for each design variable.*

Based on the design geometry shown in Fig. 4, the design variables were chosen as $\theta_f \in (-25^\circ, 25^\circ)$

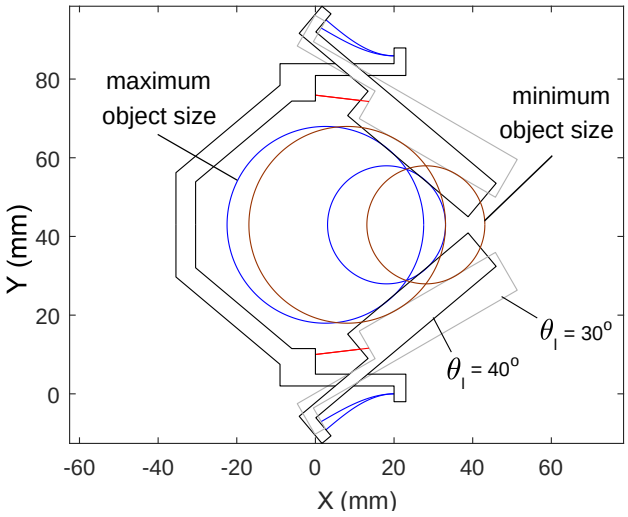


Figure 11: Minimum and maximum object sizes and initial link angles considered for simulation and optimization.

and $t \in (0.2, 0.4)$ mm, as this was considered to be a practical range for fabrication. The flexure thickness was restricted to $t \geq 0.2$ mm to avoid excessively low joint stiffness and hence maintain joint stability in unconstrained conditions and reduce out-of-plane twisting (as these are not explicitly accounted for in the optimization). A random population of 4000 designs were generated within this set for the two types of joint design: direct flexure and inverted flexure.

Step 2: Evaluate feasible design sets. *The population set from step 1 is evaluated by simulations of the target set of grasping tasks. Designs that do not meet the minimum requirements for grasping function (such as avoiding stress limits and maintaining grasp stability) in all tasks are eliminated. The remaining designs form the feasible design set that can be considered for identification of the optimal design.*

Feasible designs were extracted from the overall design set from step 1 by eliminating designs that experienced excessive flexure joint stress ($\sigma_{max} > \sigma_{lim}$) or loss of grasping stability ($K_e \leq 0$) in any of the nine simulated grasping tasks. The feasible design sets for both joint types are shown in Fig. 12. Designs from these sets can ensure basic grasping capability for all nine designated tasks.

Step 3: Evaluate performance metrics for feasible designs. *The identified performance metrics (to be minimized) are evaluated for each design within the feasible set and a normalization procedure undertaken to re-scale the metrics so that values fall with a range from 0 to 1. These normalized metrics can then be compared directly on a relative basis, which also has benefits for multi-criteria optimization [36].*

Three metrics were formulated based on peak flexure stress, effective grasp stiffness, and actuation cable force. To cover a range of grasping loads, these metrics were evaluated based on mean values over the total ramge ($W_0 = 0 \rightarrow \widehat{W_0}$) and normalized using minimum and maximum values over the feasible design set. The normalized metric for peak flexure stress was given by

$$\epsilon_1(\theta_f, t) = \frac{\overline{\sigma}(\theta_f, t) - \overline{\sigma}_{min}}{\overline{\sigma}_{max} - \overline{\sigma}_{min}} \tag{24}$$

where $\overline{\sigma}(\theta_f, t)$ is the mean value of the peak stress over the desired operating envelope, and $\overline{\sigma}_{max}$ and $\overline{\sigma}_{min}$ are the maximum and minimum values taken over the whole feasible design set. As minimizing compliance is equivalent to maximizing stiffness, the metric for effective grasp compliance was adopted as

$$\epsilon_2(\theta_f, t) = \frac{\overline{K}_e^{-1}(\theta_f, t) - \overline{K}_{e,min}^{-1}}{\overline{K}_{e,max}^{-1} - \overline{K}_{e,min}^{-1}} \tag{25}$$

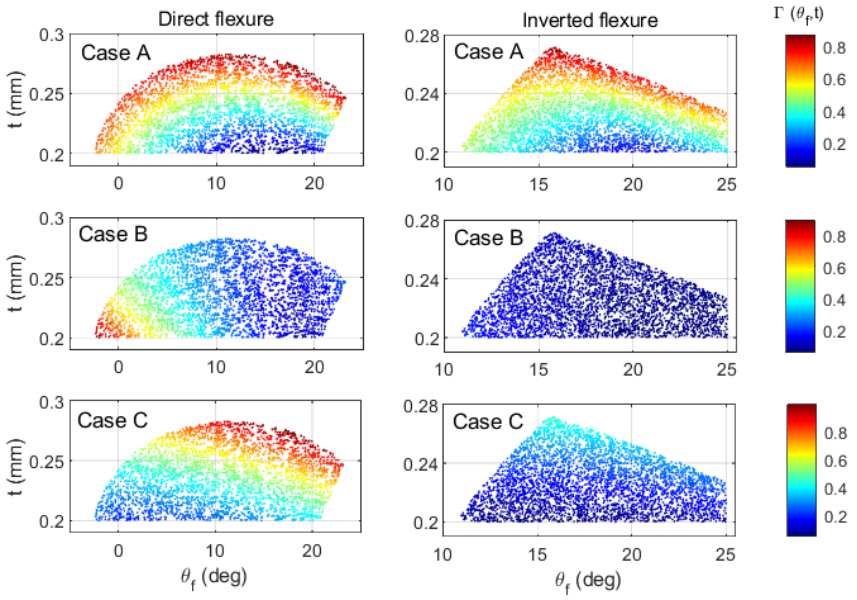


Figure 12: Objective function values for direct and inverted flexure gripper designs within the feasible sets.

Similarly, the metric for mean cable force was calculated as

$$\epsilon_3(\theta_f, t) = \frac{\overline{T}(\theta_f, t) - \overline{T}_{min}}{\overline{T}_{max} - \overline{T}_{min}} \tag{26}$$

To evaluate these normalized metrics only one (median) grasping task was considered, for which the initial finger angle was 35° and the object size was $R = 20$ mm.

Step 4: Perform search-based optimization. *An objective function* Γ *is defined based on the weighted-sum method [37], using the normalized metrics from step 3, and a search-based method used to find the optimal design within the feasible set, i.e. the design giving the minimum value of* Γ.

For the test case problem, the objective function was defined as

$$\begin{aligned} \Gamma(\theta_f, t) &= w_1\epsilon_1 + w_2\epsilon_2 + w_3\epsilon_3, \\ w_1 + w_2 + w_3 &= 1, \text{ and } w_1, w_2, w_3 > 0 \end{aligned} \tag{27}$$

where the weighting factors w_1, w_2 and w_3 were chosen to adjust the trade-off between each performance metric. The first weighting w_1 penalizes maximum stress, w_2 penalizes grasp compliance and w_3 penalizes cable actuation force.

To broadly compare the direct flexure and inverted flexure designs, three optimization cases (A, B, and C) were chosen with the different weighting factors shown in Table 2. Design cases A focus on minimizing stress, while cases B focus on maximizing grasp stiffness. Cases C represent a more typical design for a flexure-based gripper that accounts for flexure stress and cable force but neglects grasp stiffness/stability (e.g. as in [3]). Values of the objective function are shown in Fig. 12 for cases A, B and C. A discussion of the optimal design solutions having minimum values of Γ follows in Section 4.2.

In the present work, a large initial population was generated by uniform random distribution. Therefore, a near-optimal design could be obtained by direct evaluation of every design within the steps 2, 3 and 4. For problems that involve a larger number of design parameters, or more complex simulations, this approach may become infeasible due to longer computation times. However, in such cases, population-based search methods, such as particle swarm optimization or genetic algorithms [38], could be employed to improve efficiency. In practice, alternative formulations of the design optimization problem could also be used. For

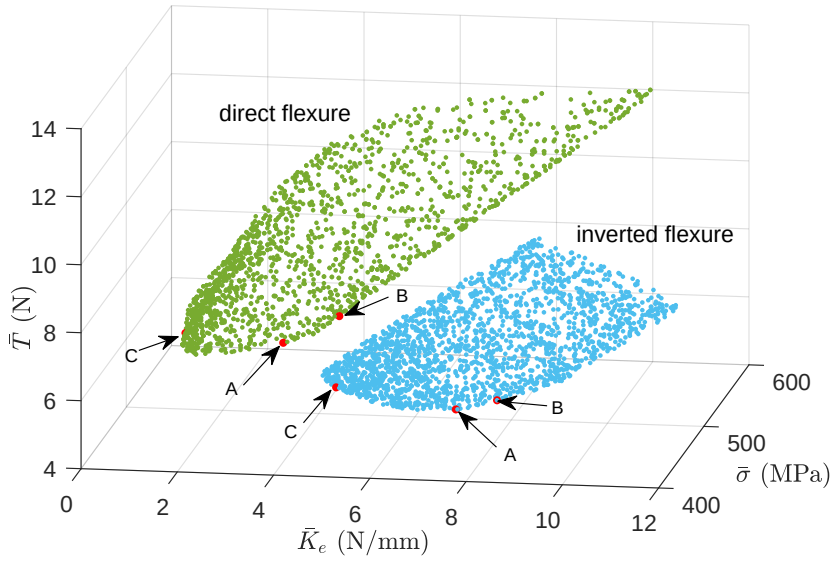


Figure 13: Achievable performance metrics for direct and inverted flexure gripper designs within the feasible sets shown in Fig. 12.

Table 2: Optimal design solutions for different performance weightings.

Case	**Weighting factors**			**Results**					
				Direct flexure			Inverted flexure		
	w_1	w_2	w_3	θ_f (deg)	t (mm)	Γ	θ_f (deg)	t (mm)	Γ
A	0.8	0.1	0.1	16.3	0.2	0.05	20.7	0.2	0.13
B	0.1	0.8	0.1	18.7	0.2	0.13	22.3	0.2	0.04
C	0.1	0.0	0.9	0.0	0.2	0.19	13.0	0.2	0.04

example, an inequality constraint could be applied to one metric, while the other two are minimised in a weighted-sum sense. This may be useful, for example, when the maximum available actuation force is known, and the design optimization should be made subject to this constraint.

4.2. Optimization results

Table 2 shows the optimal design solutions (θ_f and t) for each case: A, B and C. Performance metrics for each optimal design are shown in Table 3. The six optimal designs are also indicated by points A, B, and C in Fig. 13, which shows the achievable performance for all designs from the feasible set. It can be seen that these solutions are also optimal in a multi-objective sense, as they are all boundary points within the Pareto-optimal front, i.e. designs for which one metric can be decreased only by increasing one or more of the other two metrics [39].

Overall, the inverted flexure designs exhibit higher flexure stress, but have significantly improved grasp stiffness and lower cable force (see Table 3). The stress variation over the the range of object loads is shown in Fig. 14a. The grasp stiffness and cable force variation are shown in Fig. 14b and 14c, respectively. Peak stress values were similar for the two design types in each optimization case (with differences within 10 %). However, the effective grasp stiffness was significantly higher for the inverted flexure design, especially at the largest object load of 3 N, for which grasp stiffness values are over double those of the direct flexure designs (Fig. 14b). It is noteworthy that an increase in grasp stiffness is associated with an increase in flexure angle for both design types. Not surprisingly, optimization case C, in which grasp stiffness is neglected, results in

Table 3: Performance metrics for optimal design solutions in Table 2.

Case	Direct flexure design			Inverse flexured design		
	$\overline{\sigma}$ (MPa)	$\overline{K}_e$ (N/mm)	$\overline{T}$ (N)	$\overline{\sigma}$ (MPa)	$\overline{K}_e$ (N/mm)	$\overline{T}$ (N)
A	439	3.90	7.18	462	7.20	4.94
B	453	4.87	7.75	475	7.94	5.03
C	525	1.00	5.77	510	4.30	4.06

very low effective grasp stiffness for the direct flexure design: the peak value is 1.20 N/mm compared with 6.75 N/mm for the inverted flexure design. The lower cable tension for the inverted flexure designs can be explained by the fact that the distance between the joint's instantaneous center of rotation and cable line of action is larger than for the direct flexure design. Therefore, the inverted flexure design requires lower cable force to produce a balancing moment for the object contact force.

Case C for the inverted flexure design matches the hardware setup previously used for model validation. The cable actuation force and flexure strains were not measured in the experiments. However, the grasp performance can be evaluated directly from the measured object load-displacement behavior. To compare with the predicted values of effective grasp stiffness, a polynomial approximation was first applied to the experimental data in Fig. 10. A 3$^{\text{rd}}$ order polynomial was adopted, as this gave reasonable approximation accuracy without indication of over-fitting. The effective grasp stiffness was then calculated as the derivative of the approximating function. The results shown in Fig. 15 are compared with two theoretical curves. The model used for the optimization does not account for link compliance, and so the grasp stiffness of the experimental gripper is lower (by up to 13 % at the highest load). However, with the previously suggested link attachment compliance ($C_l = 0.0017$ mm/N), the results are in much closer agreement and confirm that significantly higher stiffness values can still be achieved compared with the equivalent conventional jointed design.

5. Application study and comparisons

Further experiments were performed to confirm the manufacturability and operating performance of the inverted flexure gripper design, and to provide further comparison with a counterpart direct-flexure grippers. Test articles were fabricated with the structure shown in Fig. 16. Both design versions used two parallel carbon fiber plates of 1 mm thickness, between which the fixed link was clamped, thereby forming a 'sandwich' structure for the palm link. The other main parts were made by 3-D printing in PLA with flexures bonded into slots using cyanoacrylate adhesive. The actuation cables were made from carbon fiber strands and were actuated using lead screw mechanisms. The overall geometry matched that previously defined in Table 1. The process of manufacturing the two grippers was very similar, although, for the inverted flexure gripper, the palm link was split into three parts in order to create gaps through which the flexure could pass to connect with the finger links. The overall dimensions of the two gripper designs, in the undeflected configuration, were almost identical.

The flexure material was chosen as pressed stainless steel of grade SUS 304H, which is commonly available in the form of shim tape. This material exhibits a high yield stress of approximately 1 GPa and has a Youngs modulus $E = 200$ GPa. With regard to the issue of material selection, it is useful to recognize that the flexure elastic forces scale with the modulus of the flexure material. Therefore, a theoretical deformation solution (and hence strain) will be unchanged when the external forces are scaled by the same factor as E (assuming friction is unchanged and link compliance is negligible) i.e. the same elastokinematic solutions is valid. This is evident by comparing the simulation results for stainless steel ($E = 200$ GPa) with target load 4.8 N and the previous results for beryllium copper ($E = 125$ GPa) with target load 3.0 N, as shown in Fig. 17. It can be seen that the peak strains for these two cases are the same i.e. for a given joint geometry, the peak strain does not depend on the flexure material. Moreover, if the maximum allowed strain for the two materials is the same then the feasible design sets will be the same. In consequence, the optimum geometry

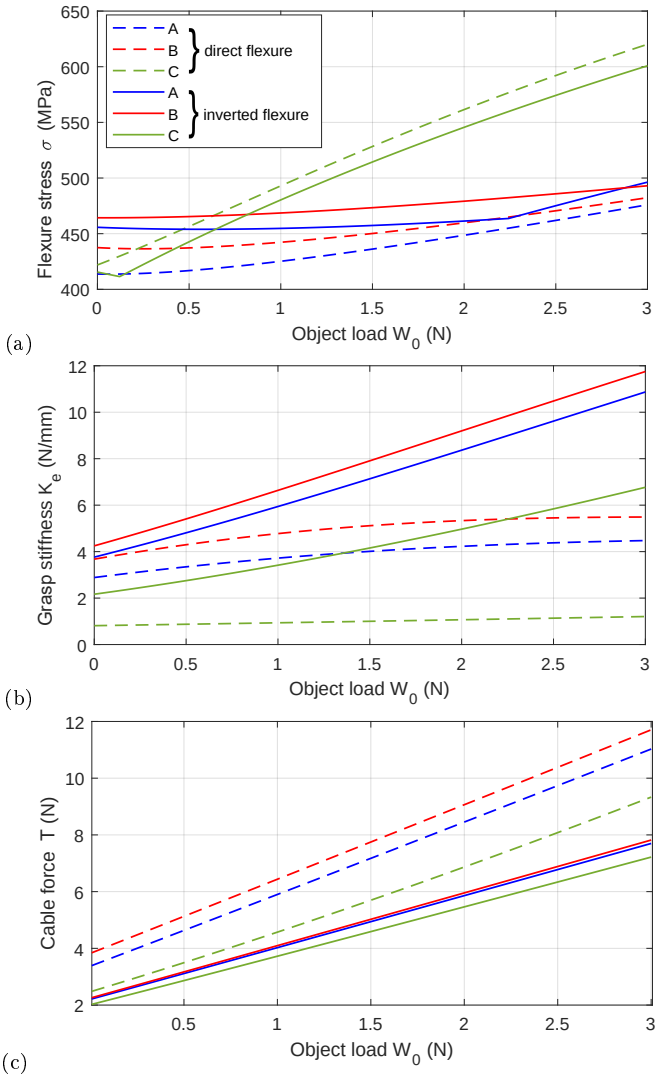


Figure 14: Gripper behaviours over range of object loads for optimal designs A, B and C: (a) peak flexure stress (b) effective grasp stiffness and (c) cable tension force.

for a design based on the previously defined force/stress metrics is not strongly dependent on the choice of flexure material, even though the resulting values of the metrics may be.

During testing, the grippers were operated in the vertical plane subject to gravity loading of the circular object, applied by connecting to a container that was slowly filled with water, as illustrated in Fig. 18. Three different designs were tested, as detailed in Table 4. The main purpose of these tests was to confirm the maximum load without yielding or loss-of-grasp, and check consistency with the model-based theory. Unlike the more precise validation tests described in Section 3, for which the object displacement was controlled and the load force measured, in these tests, the load force was the controlled variable. Consequently, the object tended to undergo small slip-stick motions caused by friction, making precise continuous measurement of the load-displacement response more difficult. Object motion and loading was recorded continuously by video and post-processed. Results are shown in Fig. 19 for the direct flexure and inverted flexure designs, both having flexure angle $\theta_f = 20°$ and thickness $t = 0.1$ mm. The model-based predictions and experimental results show good consitency for these tests. The stability limit (maximum load) for the direct-flexure case was very close to the theoretical value, as indicated by the point where $dW_0/dx_0 = 0$. [A video clip for these

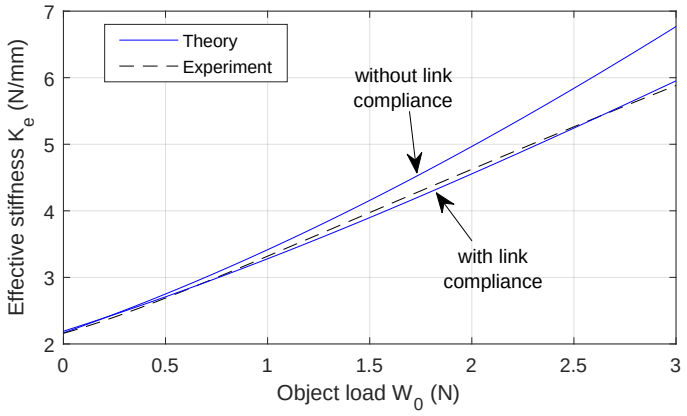
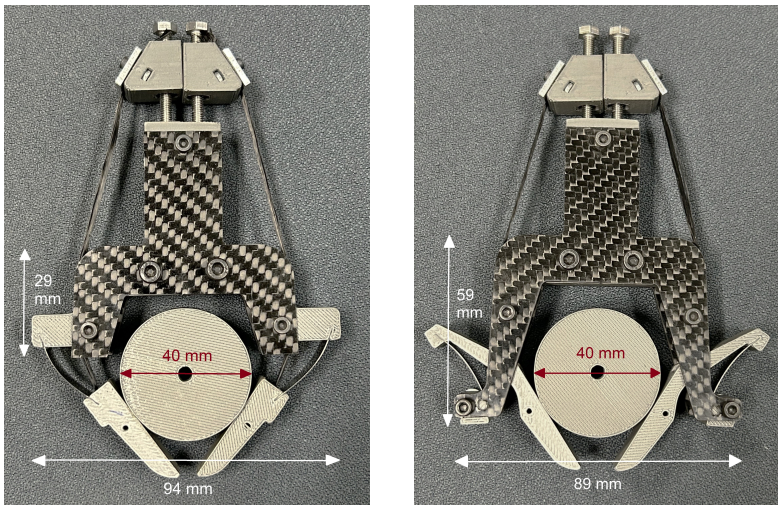


Figure 15: Theoretical and experimental results for optimized design case C showing effective grasp stiffness K_e versus object load.



(a) (b)

Figure 16: Fabricated test articles used in vertical loading tests: (a) direct flexure gripper design (b) inverted flexure gripper design.

tests is provided separately]

The full set of results is summarised in Table 4. Case 1 is a direct flexure gripper with a flexure angle of 17° and thickness of 0.15 mm, and is a near-optimal design for stress minimization (see Fig. 5a). The maximum predicted load without yielding is 9.8 N for both initial configurations with 30° and 40° finger angles. When testing the 30° case, loss-of-grasp occured at a load of 10.3 N. This is slightly lower than the predicted value owing to the occurrence of yielding before the stability limit was reached. For the 40° case, the stability limit was not reached and slight yielding was evident at the maximum tested load. Case 2 involved a direct flexure gripper with flexure thickness of 0.1 mm. This case was chosen for its low stiffness/stability properties with a view to model validation, as previously discussed and presented in Fig. 19. For this case, the experimental stability limits were slightly higher than the theoretical values, likely due to stiction at the object contact points. Yielding of the flexure material was not evident. Case 3 involved an inverted-flexure gripper with the same joint parameters as case 2. This case exhibited no instability and could support higher maximum load than the direct-flexure cases. No yielding was detected at the maximum tested load of 10.8 N. An important observation from these tests is that, for the direct flexure

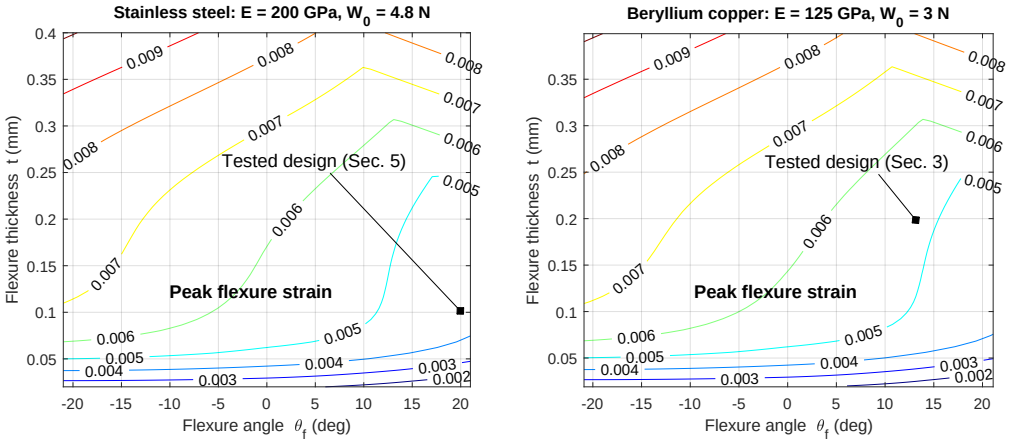


Figure 17: Contours of equivalue peak flexure strain over the design space. Simulation results are for the inverted flexure gripper with initial finger angle of 40° and object radius of 20 mm: (a) stainless steel flexure material (E = 200 GPa) (b) beryllium copper flexure material (E = 125 GPa).

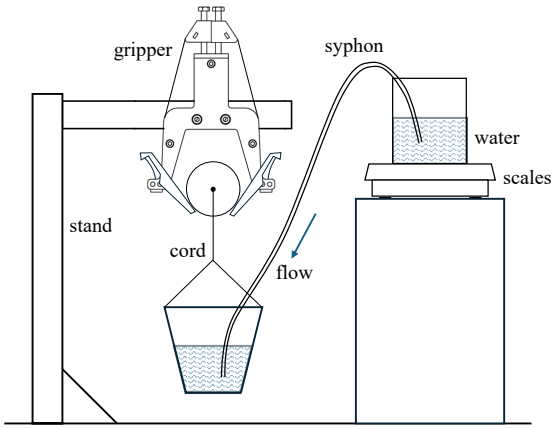


Figure 18: Schematic diagram of experimental setup for vertical loading tests.

gripper, yielding of the flexure material tends to reduce the stability limit and cause the gripper to fail with loss-of-grasp. However, for the inverted-flexure gripper, yielding did not result in loss-of-grasp.

6. Conclusions

This paper has considered the application of an inverted flexure joint design to enhance the performance characteristics of a cable-driven compliant gripper mechanism. An energy-based approach was developed to predict kinetostatic behavior based on a grasped-object interaction model and further applied for multi-objective design optimization. The results show that the inverted flexure design can significantly improve mean grasp stiffness - by more than 63 % compared with the direct flexure design - in a targeted design optimization (case B). Additionally, the cable force for the inverted flexure designs was reduced by over 20 % in all cases.

Experimental evaluations were made of a specific inverted flexure design using a specially designed test rig. The results showed good agreement with the model-based predictions, although a slightly lower grasp

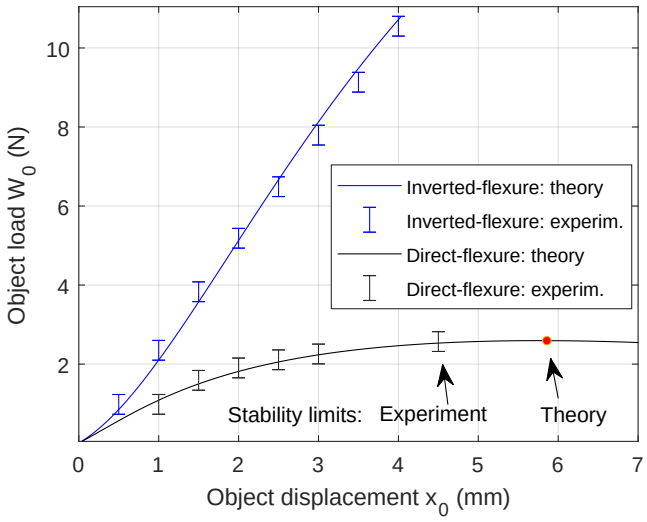


Figure 19: Object load-displacement behaviour for test article grippers: direct-flexure and inverted-flexure designs with $\theta_f = 20°$ and $t = 0.1$ mm. The initial finger angle was 30°. [A video clip for these tests is provided separately]

Table 4: Grasping test results for selected design cases.

Design case	**Flexure param.** θ_f (deg)	t (mm)	**Initial finger angle** (deg)	**Model-based results** Stability limit load (N)	Yield limit load (N)	**Experimental results** Stability limit load (N)	Maximum tested load (N)	Yielding at maximum tested load
1. Direct flexure	17	0.15	30	11.8	9.8	10.3	10.3	Visible yielding
			40	17.0	9.8	not reached	10.3	Visible yielding
2. Direct flexure	20	0.10	30	2.6	2.6	2.6	2.6	Not detected
			40	4.0	3.7	4.3	4.3	Not detected
3. Inverted flexure	20	0.10	30	-	21.8	-	10.8	Not detected
			40	-	10.5	-	10.8	Not detected

stiffness was measured ($\leq 13\,\%$), attributable to unmodelled link compliance. Further experiments performed on fabricated grippers under gravity loading of the grasped object confirmed the predicted operating performance. Unlike the direct flexure design, loss-of-grasp instability was avoided, even during overload conditions when flexure yielding occurred. A main limitation of the analysis and optimization approach in the present work is that only in-plane motion was considered. Future work should focus on the design of more general gripper architectures with inverted flexure joints, such as three-finger grippers, and consider more complete 3-D object interaction geometries for analysis and optimization.

Acknowledgement

This work was supported by Chiang Mai University Fundamental Fund 2023 [FF66/058].

Appendix: Position vector definitions

For the constraint equations (15)-(17), the cable attachment point N in the global frame is related to the finger link position according to:

$$\boldsymbol{p}_N(\boldsymbol{z}_i) = \begin{bmatrix} x_i \\ y_i \end{bmatrix} + \widetilde{R}_{2x2}(\theta_i) \begin{bmatrix} -a_0 \\ b_0 \end{bmatrix}$$

where a_0 and b_0 are the offsets for the finger link frame, as shown in Fig. 4. Similarly, the global position of the flexure root frame can be related to the position of the connecting finger link $z_i = [x_i, y_i, \theta_i]^T$ according to:

$$\boldsymbol{s}_k^r(\boldsymbol{z}_i) = \begin{bmatrix} x_i \\ y_i \\ \theta_i \end{bmatrix} + \widetilde{R}(\theta_i) \begin{bmatrix} -a_0 - a_j \\ b_0 - b_j \\ \theta_f \end{bmatrix}$$

The position vectors $\boldsymbol{p}_M(\boldsymbol{z}_1)$ and $\boldsymbol{s}_k^t(\boldsymbol{z}_1)$ correspond to fixed points on the palm link and can be defined relative to global frame $\{G\}$ using the geometric parameters in table 1.

References

[1] A. M. Dollar and R. D. Howe, "The highly adaptive SDM hand: Design and performance evaluation," *Int. J. Robot. Res.*, vol. 29, no. 5, pp. 585–597, 2010.

[2] C.-H. Liu, F.-M. Chung, Y. Chen, C.-H. Chiu, and T.-L. Chen, "Optimal design of a motor-driven three-finger soft robotic gripper," *IEEE/ASME Trans. Mechatron.*, vol. 25, no. 4, pp. 1830–1840, 2020.

[3] L. Garcia, M. Naves, and D. M. Brouwer, "3D-printed flexure-based finger joints for anthropomorphic hands," in *Proceedings of 2018 IEEE/RSJ International Conference on Intelligent Robots and Systems (IROS)*, 2018, pp. 1437–1442.

[4] K. Folkersma, S. Boer, D. Brouwer, J. Herder, and H. Soemers, "A 2-DOF large stroke flexure based positioning mechanism," in *IDETC/CIE 2012*, 2012, pp. 221–228.

[5] S. Terrile, M. Argüelles, and A. Barrientos, "Comparison of different technologies for soft robotics grippers," *Sensors*, vol. 21, no. 9, p. 3253, 2021.

[6] R. R. Ma, L. U. Odhner, and A. M. Dollar, "A modular, open-source 3D printed underactuated hand," in *Proceedings of 2013 IEEE International Conference on Robotics and Automation*, 2013, pp. 2737–2743.

[7] K. Tai, A.-R. El-Sayed, M. Shahriari, M. Biglarbegian, and S. Mahmud, "State of the art robotic grippers and applications," *Robotics*, vol. 5, no. 2, pp. 1–20, 2016.

[8] J. Shintake, V. Cacucciolo, D. Floreano, and H. Shea, "Soft robotic grippers," *Adv. Mater.*, vol. 30, no. 29, p. 1707035, 2018.

[9] Festo Ltd., *Adaptive gripper fingers DHAS*, 2023. [Online]. Available: https://www.festo.com/media/pim/049/D15000100122049.PDF

[10] G. Salvietti, I. Hussain, M. Malvezzi, and D. Prattichizzo, "Design of the passive joints of underactuated modular soft hands for fingertip trajectory tracking," *IEEE Robot. Autom. Lett.*, vol. 2, no. 4, pp. 2008–2015, 2017.

[11] M. Liarokapis and A. M. Dollar, "Combining analytical modeling and learning to simplify dexterous manipulation with adaptive robot hands," *IEEE Trans. Autom. Sci. Eng.*, vol. 16, no. 3, pp. 1361–1372, 2019.

[12] I. Hussain, M. Malvezzi, D. Gan, Z. Iqbal, L. Seneviratne, D. Prattichizzo, and F. Renda, "Compliant gripper design, prototyping, and modeling using screw theory formulation," *Int. J. Robot. Res.*, vol. 40, no. 1, pp. 55–71, 2021.

[13] L. U. Odhner, L. P. Jentoft, M. R. Claffee, N. Corson, Y. Tenzer, R. R. Ma, M. Buehler, R. Kohout, R. D. Howe, and A. M. Dollar, "A compliant, underactuated hand for robust manipulation," *Int. J. Robot. Res.*, vol. 33, no. 5, pp. 736–752, 2014.

[14] M. Tavakoli, A. Sayuk, J. Lourenco, and P. Neto, "Anthropomorphic finger for grasping applications: 3D printed endoskeleton in a soft skin," *Int. J. Adv. Manuf. Technol.*, vol. 91, pp. 2607–2620, 2017.

[15] J. Guo and K.-M. Lee, "Compliant joint design and flexure finger dynamic analysis using an equivalent pin model," *Mech. Mach. Theory*, vol. 70, pp. 338–353, 2013.

[16] Y. Zhang, Q. Zhan, R. Li, and X. Bao, "Design, fabrication and experiments of an anthropomorphic finger with combined compliant joints," *J. Bionic Eng.*, vol. 17, pp. 1152–1162, 2020.

[17] M. Cutkosky and I. Kao, "Computing and controlling compliance of a robotic hand," *IEEE Transactions on Robotics and Automation*, vol. 5, no. 2, pp. 151–165, 1989.

[18] G. A. Kragten, M. Baril, C. Gosselin, and J. L. Herder, "Stable precision grasps by underactuated grippers," *IEEE Trans. Robot.*, vol. 27, no. 6, pp. 1056–1066, 2011.

[19] A. S. Vazquez, I. Payo, R. Fernandez, J. Becedas, and J. J. Jimenez, "Design parameters of flexible grippers for grasping," in *Proceedings of IEEE International Conference on Robotics and Automation*, 2013, pp. 2060–2066.

[20] B. Okken, J. P. Dekker, J. J. de Jong, and D. M. Brouwer, "Numerical optimization of underactuated flexure-based grippers," in *Proceedings of IDETC/CIE*, 2023, p. V008T08A041.

[21] B. P. Trease, Y.-M. Moon, and S. Kota, "Design of large-displacement compliant joints," *J. Mech. Des.*, vol. 127, no. 4, pp. 788–798, 2004.

[22] F. Chen, W. Xu, H. Zhang, Y. Wang, J. Cao, M. Y. Wang, H. Ren, J. Zhu, and Y. F. Zhang, "Topology optimized design, fabrication, and characterization of a soft cable-driven gripper," *IEEE Robot. Autom. Lett.*, vol. 3, no. 3, pp. 2463–2470, 2018.

[23] R. R. Ma and A. M. Dollar, "Linkage-based analysis and optimization of an underactuated planar manipulator for in-hand manipulation," *J. Mech. Robot.*, vol. 6, no. 1, p. 011002, 2013.

[24] C. Rotinat-Libersa and B. Solano, "Optimal design of compliant joint and gripper for miniature robotic devices: Application to surgery," in *Proceedings of IDETC/CIE*, 2012, pp. 393–402.

[25] P. Kuresangsai, M. O. T. Cole, and G. Hao, "Grasp stability and design analysis of a flexure-jointed gripper mechanism via efficient energy-based modeling," *IEEE Robot. Autom. Lett.*, vol. 7, no. 4, pp. 12 499–12 506, 2022.
[26] A. E. Guérinot, S. P. Magleby, L. L. Howell, and R. H. Todd, "Compliant joint design principles for high compressive load situations," *Int. J. Mech. Mater. Des.*, vol. 127, no. 4, pp. 774–781, 2004.
[27] S. Li, G. Hao, Y. Chen, J. Zhu, and G. Berselli, "Nonlinear analysis of a class of inversion-based compliant cross-spring pivots," *J. Mech. Robot.*, vol. 14, no. 3, p. 031007, 2021.
[28] S. Li, G. Hao, and W. M. Wright, "Design and modelling of an anti-buckling compliant universal joint with a compact configuration," *Mech. Mach. Theory*, vol. 156, p. 104162, 2021.
[29] J. Dearden, C. Grames, B. D. Jensen, S. P. Magleby, and L. L. Howell, "Inverted L-Arm gripper compliant mechanism," *ASME. J. Med. Devices.*, vol. 11, no. 3, p. 034502, 2017.
[30] M. Verotti, A. Dochshanov, and N. P. Belfiore, "A comprehensive survey on microgrippers design: mechanical structure," *ASME J. Mech. Des.*, vol. 139, no. 6, p. 060801, 2017.
[31] M. Ling, L. L. Howell, J. Cao, and G. Chen, "Kinetostatic and dynamic modeling of flexure-based compliant mechanisms: A survey," *Appl. Mech. Rev.*, vol. 72, no. 3, p. 030802, 2020.
[32] L. U. Odhner and A. M. Dollar, "The smooth curvature model: an efficient representation of euler-bernoulli flexures as robot joints," *IEEE Trans. Robot.*, vol. 28, no. 4, pp. 761–772, 2012.
[33] P. Kuresangsai and M. O. T. Cole, "Kinematic modeling and design optimization of flexure-jointed planar mechanisms using polynomial bases for flexure curvature," *Mech. Mach. Theory*, vol. 132, pp. 80–97, 2019.
[34] T. Liu, G. Hao, J. Zhu, P. Kuresangsai, S. Abdelaziz, and E. Wehrle, "Modeling compliant bistable mechanisms: An energy method based on the high-order smooth curvature model," *International Journal of Mechanical Sciences*, vol. 275, p. 109315, 2024.
[35] N. Lobontiu, "Compliance-based modeling and design of straight-axis/circular-axis flexible hinges with small out-of-plane deformations," *Mechanism and Machine Theory*, vol. 80, pp. 166–183, 2014.
[36] O. Grodzevich and O. Romanko, "Normalization and other topics in multi-objective optimization," in *Proceedings of the Fields-MITACS Industrial Problems Workshop*, 2006, pp. 89–101.
[37] R. T. Marler and J. S. Arora, "The weighted sum method for multi-objective optimization: New insights," *Structural and Multidisciplinary Optimization*, vol. 41, no. 6, pp. 853–862, 2010.
[38] N. Gunantara, "A review of multi-objective optimization: Methods and its applications," *Cogent Engineering*, vol. 5, no. 1, p. 1502242, 2018.
[39] K. Deb, *Multi-objective Optimization*. Springer US, 2014, ch. 15, pp. 403–449.